Extratropical intraseasonal signals along the subtropical westerly jet as a window of opportunity for subseasonal prediction over East Asia in boreal summer

Tao Zhu[1] and Yang Jing[2]

[1]Key Laboratory of Environmental Change and Natural Disaster, Faculty of Geographical Science, Beijing Normal University, mergency Management, Faculty of Geographical Science, Beijing Normal University
[2]Faculty of Geographical Science, Beijing Normal University

December 7, 2022

Abstract

Previous studies suggest that boreal summer intraseasonal variations along the subtropical westerly jet (SJ), featuring quasi-biweekly periodicity, frequently modulate downstream subseasonal variations over East Asia (EA). Based on subseasonal hindcasts from six dynamical models, this study discovered that the leading two-three-week prediction skills for surface air temperature (SAT) are improved significantly in summer when the SJ has strengthened intraseasonal signals, which are best demonstrated over the eastern Tibetan Plateau, Southwest Basin, and North China. The reasons are that the enhanced quasi-biweekly wave and the associated energy dispersion along the SJ cause more regular quasi-biweekly periodic variations of downstream SAT, which potentially increase regional predictability. This study suggests not only that intraseasonal variations along the SJ could provide a window of opportunity for achieving better subseasonal prediction over EA, but also that intraseasonal waves along the SJ are crucial for improving EA subseasonal prediction.

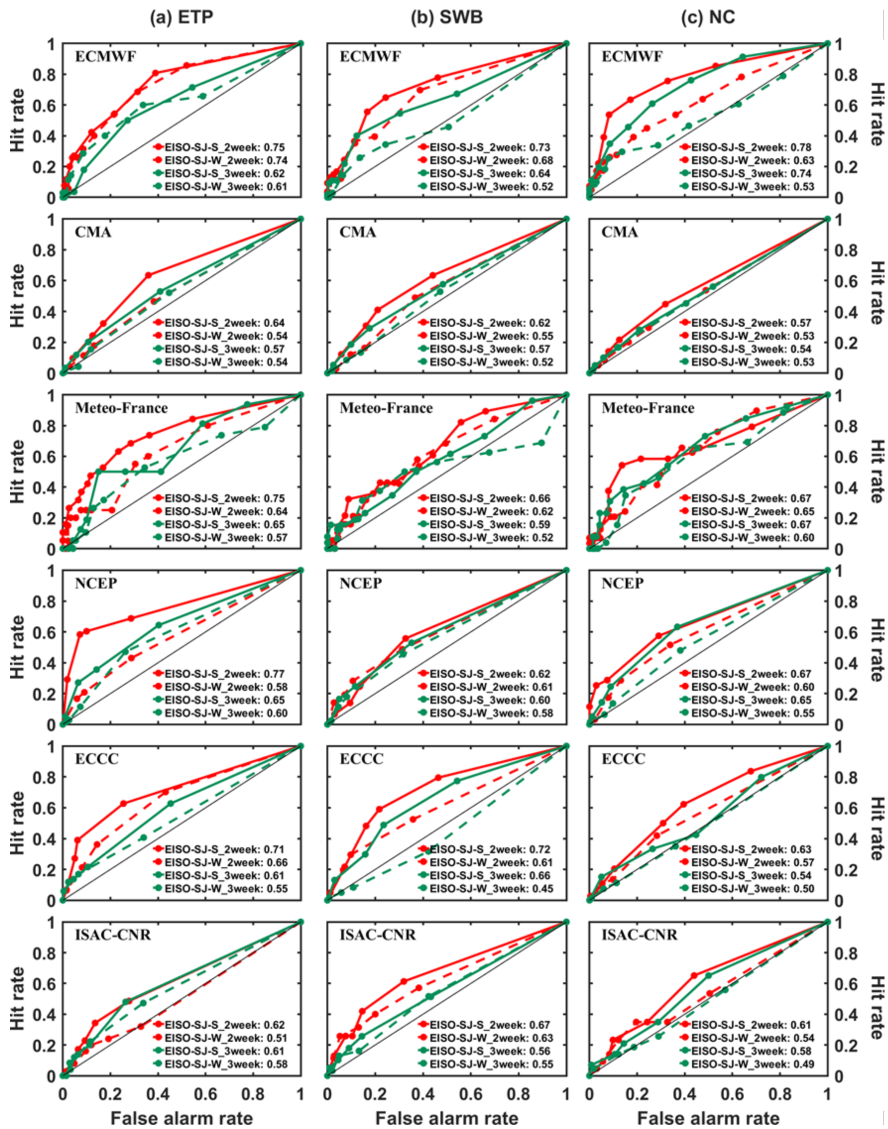
(a) ETP
(b) SWB
(c) NC
ECMWF
EISO-SJ-S_2week: 0.75
EISO-SJ-W_2week: 0.74
EISO-SJ-S_3week: 0.62
EISO-SJ-W_3week: 0.61
ECMWF
EISO-SJ-S_2week: 0.73
EISO-SJ-W_2week: 0.68
EISO-SJ-S_3week: 0.64
EISO-SJ-W_3week: 0.52
ECMWF
EISO-SJ-S_2week: 0.78
EISO-SJ-W_2week: 0.63
EISO-SJ-S_3week: 0.74
EISO-SJ-W_3week: 0.53
CMA
EISO-SJ-S_2week: 0.64
EISO-SJ-W_2week: 0.54
EISO-SJ-S_3week: 0.57
EISO-SJ-W_3week: 0.54
CMA
EISO-SJ-S_2week: 0.62
EISO-SJ-W_2week: 0.55
EISO-SJ-S_3week: 0.57
EISO-SJ-W_3week: 0.52
CMA
EISO-SJ-S_2week: 0.57
EISO-SJ-W_2week: 0.53
EISO-SJ-S_3week: 0.54
EISO-SJ-W_3week: 0.53
Meteo-France
EISO-SJ-S_2week: 0.75
EISO-SJ-W_2week: 0.64
EISO-SJ-S_3week: 0.65
EISO-SJ-W_3week: 0.57
Meteo-France
EISO-SJ-S_2week: 0.66
EISO-SJ-W_2week: 0.62
EISO-SJ-S_3week: 0.59
EISO-SJ-W_3week: 0.52
Meteo-France
EISO-SJ-S_2week: 0.67
EISO-SJ-W_2week: 0.65
EISO-SJ-S_3week: 0.67
EISO-SJ-W_3week: 0.60
NCEP
EISO-SJ-S_2week: 0.77
EISO-SJ-W_2week: 0.58
EISO-SJ-S_3week: 0.65
EISO-SJ-W_3week: 0.60
NCEP
EISO-SJ-S_2week: 0.62
EISO-SJ-W_2week: 0.61
EISO-SJ-S_3week: 0.60
EISO-SJ-W_3week: 0.58
NCEP
EISO-SJ-S_2week: 0.67
EISO-SJ-W_2week: 0.60
EISO-SJ-S_3week: 0.65
EISO-SJ-W_3week: 0.55
ECCC
EISO-SJ-S_2week: 0.71
EISO-SJ-W_2week: 0.66
EISO-SJ-S_3week: 0.61
EISO-SJ-W_3week: 0.55
ECCC
EISO-SJ-S_2week: 0.72
EISO-SJ-W_2week: 0.61
EISO-SJ-S_3week: 0.66
EISO-SJ-W_3week: 0.45
ECCC
EISO-SJ-S_2week: 0.63
EISO-SJ-W_2week: 0.57
EISO-SJ-S_3week: 0.54
EISO-SJ-W_3week: 0.50
ISAC-CNR
EISO-SJ-S_2week: 0.62
EISO-SJ-W_2week: 0.51
EISO-SJ-S_3week: 0.61
EISO-SJ-W_3week: 0.58
ISAC-CNR
EISO-SJ-S_2week: 0.67
EISO-SJ-W_2week: 0.63
EISO-SJ-S_3week: 0.56
EISO-SJ-W_3week: 0.55
ISAC-CNR
EISO-SJ-S_2week: 0.61
EISO-SJ-W_2week: 0.54
EISO-SJ-S_3week: 0.58
EISO-SJ-W_3week: 0.49
Hit rate
False alarm rate

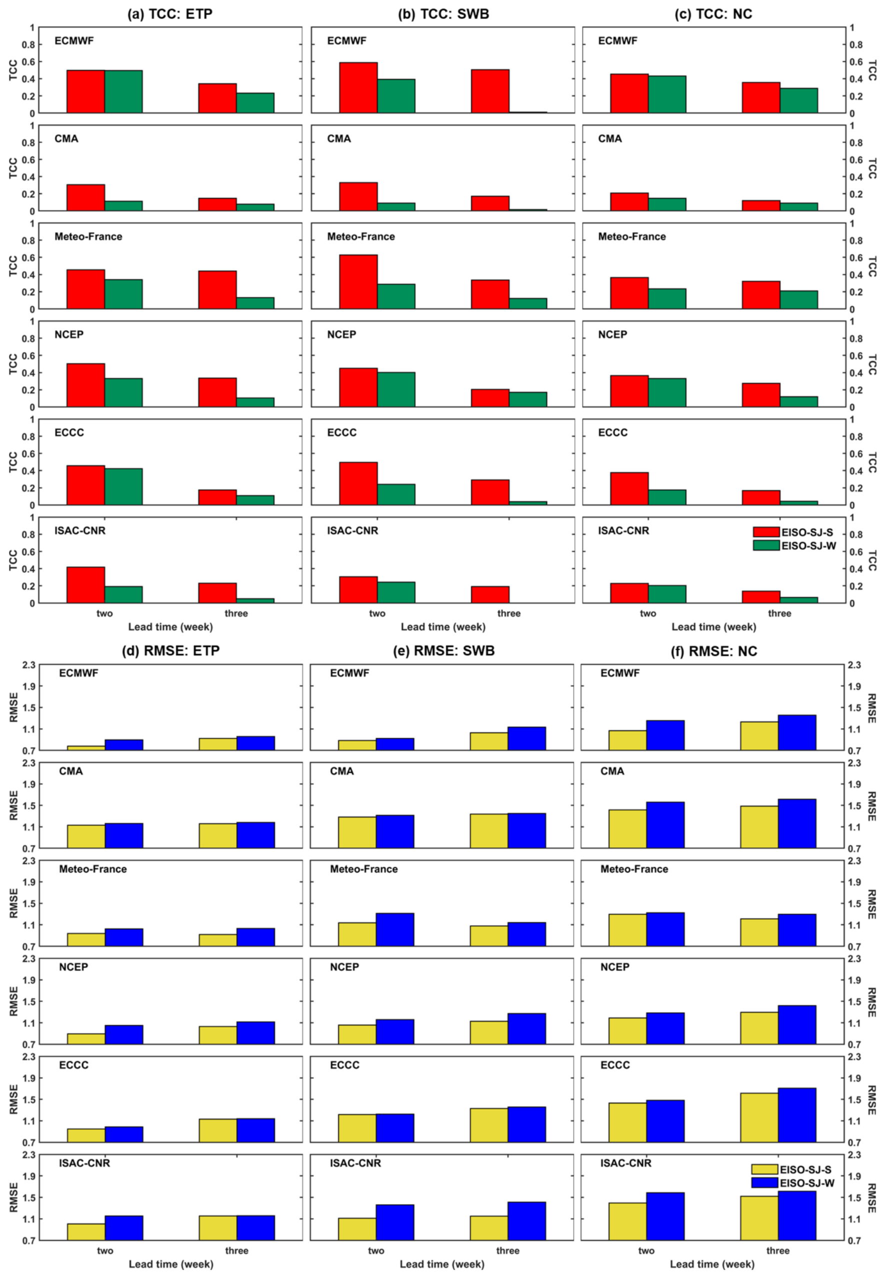
(a) TCC: ETP
(b) TCC: SWB
(c) TCC: NC
ECMWF
CMA
Meteo-France
NCEP
ECCC
ISAC-CNR
TCC
EISO-SJ-S
EISO-SJ-W
two
three
Lead time (week)
(d) RMSE: ETP
(e) RMSE: SWB
(f) RMSE: NC
RMSE

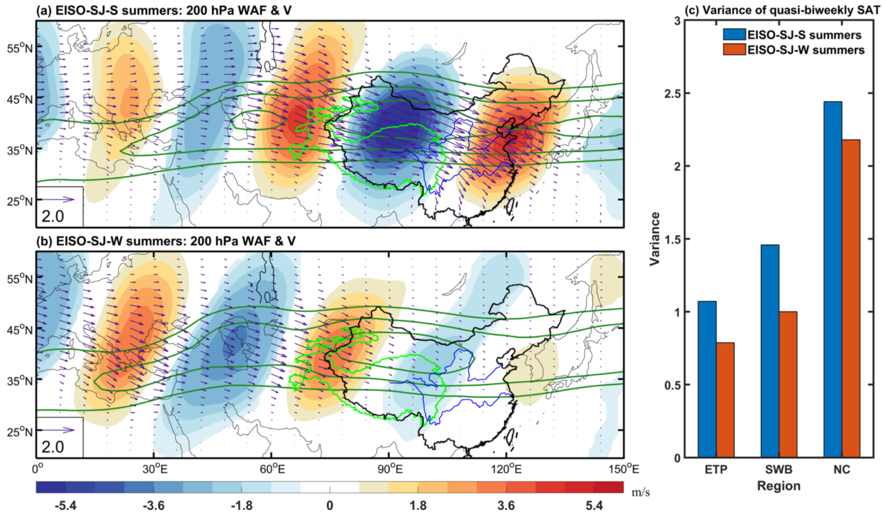
(a) EISO-SJ-S summers: 200 hPa WAF & V
(b) EISO-SJ-W summers: 200 hPa WAF & V
2.0
m/s
(c) Variance of quasi-biweekly SAT
EISO-SJ-S summers
EISO-SJ-W summers
Variance
ETP
SWB
NC
Region

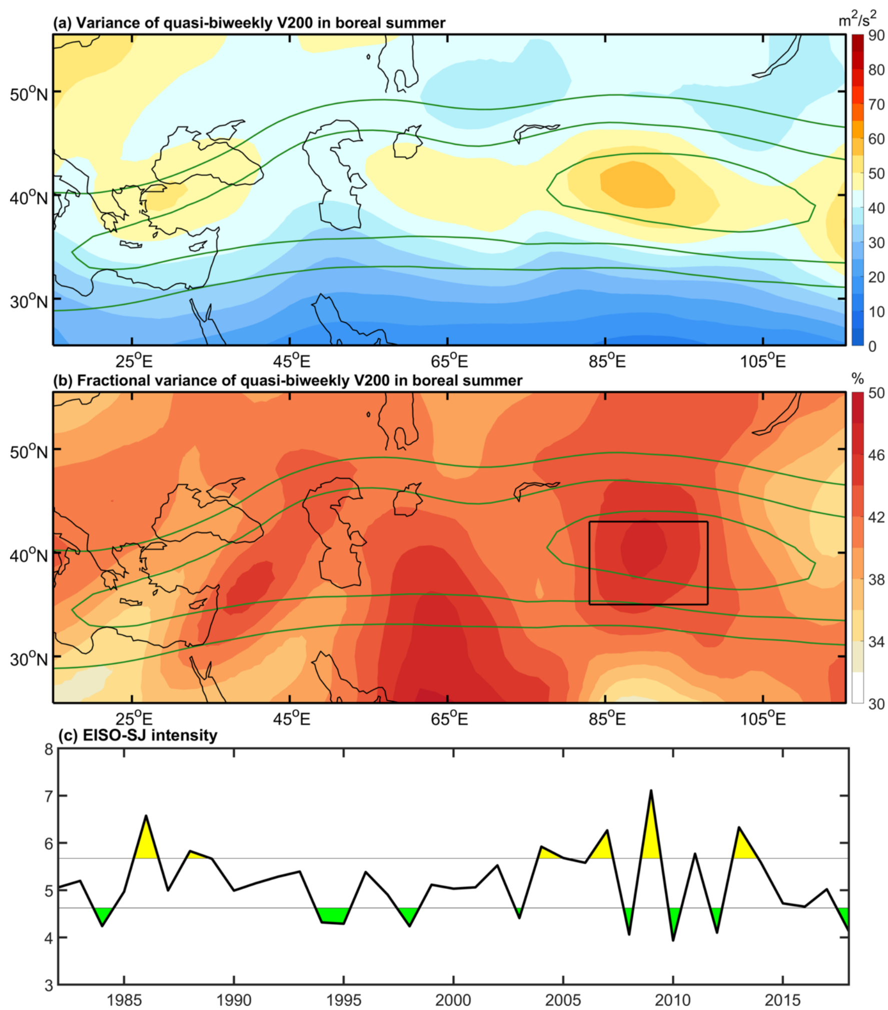
(a) Variance of quasi-biweekly V200 in boreal summer
m^2/s^2
(b) Fractional variance of quasi-biweekly V200 in boreal summer
%
(c) EISO-SJ intensity

Extratropical intraseasonal signals along the subtropical westerly jet as a window of opportunity for subseasonal prediction over East Asia in boreal summer

Tao Zhu[1,2] Jing Yang[1,2]

[1] Key Laboratory of Environmental Change and Natural Disaster, Beijing Normal University, Beijing 100875, China

[2] Faculty of Geographical Science, Beijing Normal University, Beijing 100875, China

Submitted to GRL

Nov. 2022

**Corresponding author address: Jing Yang, Key Laboratory of Environmental Change and Natural Disaster, Faculty of Geographical Science, Beijing Normal University, 19#Xinjiekouwai Street, Haidian District, Beijing 100875, China. E-mail: yangjing@bnu.edu.cn*

Abstract

Previous studies suggest that boreal summer intraseasonal variations along the subtropical westerly jet (SJ), featuring quasi-biweekly periodicity, frequently modulate downstream subseasonal variations over East Asia (EA). Based on subseasonal hindcasts from six dynamical models, this study discovered that the leading two–three-week prediction skills for surface air temperature (SAT) are improved significantly in summer when the SJ has strengthened intraseasonal signals, which are best demonstrated over the eastern Tibetan Plateau, Southwest Basin, and North China. The reasons are that the enhanced quasi-biweekly wave and the associated energy dispersion along the SJ cause more regular quasi-biweekly periodic variations of downstream SAT, which potentially increase regional predictability. This study suggests not only that intraseasonal variations along the SJ could provide a window of opportunity for achieving better subseasonal prediction over EA, but also that intraseasonal waves along the SJ are crucial for improving EA subseasonal prediction.

Key Points

- Subseasonal prediction skill over three key regions of China exhibits strong dependence on the intensity of intraseasonal variations along the subtropical westerly jet (SJ).
- Enhanced intraseasonal waves and intensified energy dispersion along the SJ increase regional surface air temperature predictability by strengthening local periodic variations.
- The intraseasonal signal along the SJ provides a window of opportunity for subseasonal prediction of regional surface air temperature during boreal summer.

Plain Language Summary

Conventional opinion considers extratropical atmospheric perturbation as noise for subseasonal-to-seasonal predictions. However, based on six state-of-the-art subseasonal-to-seasonal hindcasts, this study established the groundbreaking result that the subseasonal surface air temperature prediction skill, in three regions of China, depends strongly on the intensity of extratropical intraseasonal variation along the subtropical westerly jet. Breaking with the established perspective that the subseasonal prediction source mainly comes from the tropical region, this study was the first to propose that extratropical intraseasonal variation could provide a window of opportunity for subseasonal prediction in regions of East Asia. The results suggest that accurately capturing and predicting periodic extratropical atmospheric signals in operational predictions will be of great importance for improving subseasonal predictions of East Asian monsoon regions.

1. Introduction

Subseasonal prediction, which is crucial for many sectors of society and for decision makers in terms of improved planning and preparations for saving lives, protecting property, and increasing economic vitality (National Academies of Sciences report 2016), is a challenging task in operational service (Robertson et al. 2015; Vitart et al. 2017). One current barrier to improved subseasonal prediction is the obscure prediction sources on this time scale. Previous studies have attempted to elucidate the subseasonal prediction sources, including tropical intraseasonal oscillations (e.g., the Madden–Julian Oscillation (MJO) and boreal summer intraseasonal oscillation (BSISO)), anomalous signals from land (soil moisture and soil temperature), snow cover, sea ice, the stratosphere, and the ocean (e.g., the El Niño–Southern Oscillation (ENSO), local sea surface temperature, and mesoscale sea surface temperature variability), which have all been reviewed comprehensively in the National Academies of Sciences report (2016) and Merryfield et al. (2020).

Skillful subseasonal prediction is particularly important over East Asia (EA), which is one of the most densely populated regions globally, accounting for 22% of the world’s population (Leung 2012). Subseasonal prediction in boreal summer over EA is challenging owing to complex interactions between tropical monsoon variability and mid–high-latitude circulation systems (Liang and Lin 2017). Previous studies proved that subseasonal prediction sources over EA include preferable phases of the MJO (Lin 2018) and BSISO (Wu et al. 2022), the ENSO state (Martin et al. 2019), snowpack (Orsolini et al. 2013; Li et al. 2020), land surface conditions (Zeng and Yuan 2018; Xie et al. 2019; Xue et al. 2021) and stratospheric signals (Yu et al. 2021). Conventional perspective considers the extratropical atmospheric perturbation as noise for prediction (Vimont et al. 2001; Zhang et al. 2018). However, along the subtropical westerly jet (SJ), remarkable periodic atmospheric intraseasonal signals, such as a quasi-biweekly oscillation, have been proven to have significant influence on the weather and climate of EA (Watanabe and Yamazaki 2012; Yang et al. 2017; Zhong et al. 2022) and even to trigger extreme events (Chan et al. 2002; Fujinamij and Yasunari 2004; Li et al. 2021).

Meanwhile, a number of recent studies have found that subseasonal prediction biases over EA are affected substantially by extratropical intraseasonal oscillations along the SJ (EISO-SJ) (Qi and Yang 2019; Yan et al. 2021, 2022). Therefore, it is worth investigating whether the atmospheric EISO-SJ, similar to the MJO/BSISO, is one of the subseasonal prediction sources over EA.

Considering the atmospheric EISO-SJ features remarkable year-to-year variation in boreal summer (Fig. S1 in the supplementary materials presents a simple example examining the year-to-year variation of the intraseasonal SJ index, calculated in accordance with the definition of Yang and Zhang (2007)), the objective of this study was to investigate whether there exists remarkable dependence of EA subseasonal prediction on the atmospheric EISO-SJ from the perspective of comparing summers with strong and weak EISO-SJ intensity, primarily based on the subseasonal-to-seasonal (S2S) hindcast dataset. The results presented in this paper are analyzed in an attempt to identify another important window of opportunity for EA subseasonal prediction.

2. Data and methods

Daily atmospheric circulation fields were retrieved from the ERA-Interim dataset provided by the European Centre for Medium-Range Weather Forecasts (ECMWF) (Dee et al., 2011). The horizontal resolution of the gridded data was 1.5° × 1.5° and the historical record covered 1982–2018. Daily surface air temperature (SAT) and precipitation data (1982–2018) recorded at 2479 observing stations in China were obtained from the China Meteorological Administration. Here, boreal summer is defined as May 1 to August 31.

For the S2S reforecast data, the hindcast from the database of the S2S prediction project was used (Virart et al. 2017), in which six models were analyzed: the China Meteorological Administration (CMA), the European Center for Medium-Range Forecast (ECMWF), the Environment and Climate Change Canada (ECCC), the Institute of Atmospheric Sciences and Climate of the National Research Council (ISAC-CNR), the Meteo-France/Centre National de Recherche Meteorologiques

(Meteo-France), and the National Centers for Environmental Prediction (NCEP). A detailed description of each of the six models is presented in Table S1 in the supplementary materials. Note that the purpose of this study was not to compare model prediction skill, but to understand the dependence of EA subseasonal prediction on the atmospheric EISO-SJ. Therefore, there was no requirement for the reforecast period, frequency of initialization, and ensemble size of the models to be uniform. Also note that the prediction skills for weekly SAT and precipitation were our targets, for which the weekly hindcast data could be obtained from the 7-day mean of the raw prediction data. For example, a two-week (three-week) prediction corresponds to the average of the forecast 11–17 (18–24) days.

The intraseasonal component of a particular variable can be obtained by the following two steps: I) subtracting the climatological mean and the first three harmonics, and II) taking a 5-day running mean. The quasi-biweekly (8–25 days in this study) component can be retrieved easily using the Butterworth bandpass filter. The statistical methods used in this study included empirical orthogonal function analysis and power spectrum analysis. A two-tailed Student's t test was used to assess statistical significance. Evaluation methods included the temporal correlation skill (TCC), root mean square error (RMSE), and relative operating characteristics (ROC) curve, which are the primary and most commonly used methods for evaluating the prediction skill of S2S models (Black et al. 2017; Wu et al. 2017; Osman and Alvarez 2018). A larger (smaller) TCC (RMSE) value represents better deterministic prediction skill, and a larger value of the area under the ROC curve (named ROCA), denotes better probabilistic prediction skill. Full details of the calculation methods can be found in Table S2 and Eqs. (S1) and (S2) in the supplementary materials. Two-dimensional wave activity flux, which is used to represent the energy dispersion of a Rossby wave, was calculated with reference to Takaya and Nakamura (2001).

3. Remarkable year-to-year variation in EISO-SJ intensity

Similar to some previous studies on the year-to-year variation of intraseasonal oscillation (e.g., Teng and Wang 2003; Moon et al. 2011; Qin et al. 2022), EISO-SJ intensity is measured by the standard deviation of boreal summer quasi-biweekly 200 hPa meridional wind (V200) averaged over the SJ core region (35°–43°N, 83°–98°E; shown by the black rectangle in Fig. 1b), i.e., the maximum center of both quasi-biweekly V200 variance and fractional variance (nearly 45% of the total variance) (Figs. 1a and 1b). In this study, V200 was chosen as the typical variable for representing the EISO-SJ because it features more prominent intraseasonal signals than other circulation fields (e.g., 200 hPa geopotential height (GHT200) and zonal wind (U200)) along the SJ (Figs. S2a–f in the supplementary materials). The quasi-biweekly component was extracted to represent intraseasonal V200 because it is the most dominant intraseasonal periodicity according to the power spectra of the circulation fields along the SJ (Fig. S2g in the supplementary materials).

Figure 1c displays the year-to-year variation of EISO-SJ intensity. First, EISO-SJ intensity exhibits significant year-to-year variation, in which the difference between the maximum and minimum value is 3.18, which represents 72.5% of the total V200 intensity (4.39). Second, EISO-SJ intensity has a significant relationship with the year-to-year change in total V200 intensity along the SJ, for which the correlation coefficient is up to 0.51, far exceeding the 99% significance level. Meanwhile, the year-to-year fractional variance of EISO-SJ intensity (variance: 0.56 $m^2\ s^{-2}$) against the total V200 intensity (variance: 0.87 $m^2\ s^{-2}$) is 64.0%. The above results show that EISO-SJ intensity has large year-to-year variation that is highly consistent with the year-to-year variation of total V200 intensity.

To probe the dependence of EA subseasonal prediction on the atmospheric EISO-SJ, two contrasting groups of summers were evaluated for each specific S2S model: strong EISO-SJ summers (EISO-SJ-S) and weak EISO-SJ summers (EISO-SJ-W). Taking the ECMWF as an example, because the reforecast period is 1996–2015 and the frequency of initialization is twice a week, the five strongest EISO-SJ intensity summers (2004, 2007, 2009, 2011, and 2013) in terms of the observations were chosen for the EISO-SJ-S group, and the five weakest EISO-SJ intensity summers (1998, 2003, 2008, 2010, and 2012) in terms of the observations were taken as the EISO-SJ-W group.

The sample size of each group was 175 (5 years × 35 times year^{-1}). Analysis for the other models followed similar methods and detailed descriptions can be found in Table S1 in the supplementary materials. To ensure distinct differences between the two groups and to maintain adequate sample sizes, the selected EISO-SJ-S and EISO-SJ-W summers exceeded a threshold of at least 0.7 times the standard deviation.

4. Dependence of subseasonal prediction for EA SAT on the EISO-SJ

Previous observational studies reported that atmospheric EISO-SJ is crucial for subseasonal variation in EA SAT (Watanabe and Yamazaki 2014; Gao et al. 2017). Therefore, in this section, we first focus on exploring the differences in the subseasonal prediction skill for EA SAT between the EISO-SJ-S and EISO-SJ-W summers. Comparison is made for both deterministic (TCC and RMSE) and probabilistic prediction (ROC) to verify the results. Two- and three-week lead predictions are the focuses of this study because the skill beyond four weeks is poor for both groups of summers. Three typical regions are chosen (eastern Tibetan Plateau (ETP): 29°–37°N, 89°–104°E, Southwest Basin (SWB): 24°–29°N, 101°–109°E, and North China (NC): 38°–44°N, 109°–119°E; black frames in Fig. S3 in the supplementary materials) because the raw SAT anomaly over these regions exhibits significant correlation with the domain-averaged quasi-biweekly V200 over the SJ core.

4.1 Better subseasonal deterministic prediction for EA SAT in summers with strong EISO-SJ intensity

The TCC and RMSE were calculated to measure the similarity and magnitude of the error between the predicted and observed weekly SAT anomaly (Harnos et al. 2019). Figures 2a–c shows the TCCs between the observed weekly SAT anomaly and the predicted ensemble-mean anomalies with two- and three-week lead times from the six S2S models over the ETP, SWB, and NC in EISO-SJ-S and EISO-SJ-W summers. The TCCs for all six S2S models are larger for EISO-SJ-S summers than for EISO-SJ-W summers in all three regions. For a three-week lead prediction over the ETP, the TCCs are 0.34 (ECMWF), 0.15 (CMA), 0.44 (Meteo-France), 0.34 (NCEP), 0.17 (ECCC), and 0.23 (ISAC-CNR) for EISO-SJ-S summers, while 0.23 (ECMWF), 0.08 (CMA), 0.13 (Meteo-France), 0.11 (NCEP), 0.10 (ECCC), and 0.05 (ISAC-CNR) for EISO-SJ-W summers (green bars in Fig. 2a). Similarly, the TCCs for EISO-SJ-S summers decrease from 0.50 to 0.01 (ECMWF), 0.17 to 0.01 (CMA), 0.34 to 0.12 (Meteo-France), 0.20 to 0.17 (NCEP), 0.29 to 04 (ECCC), and 0.19 to −0.02 (ISAC-CNR) for EISO-SJ-W summers over the SWB (green bars in Fig. 2b), and the TCCs are reduced from 0.36 (ECMWF), 0.12 (CMA), 0.32 (Meteo-France), 0.27 (NCEP), 0.17 (ECCC) and 0.14 (ISAC-CNR) for EISO-SJ-S summers to 0.29 (ECMWF), 0.09 (CMA), 0.21 (Meteo-France), 0.12 (NCEP), 0.04 (ECCC), and 0.06 (ISAC-CNR) for EISO-SJ-W summers over NC (green bars in Fig. 2c). Similar differences can be seen clearly in the two-week lead predictions, although the differences between EISO-SJ-S and EISO-SJ-W summers are not as significant as those in three-week lead predictions (see red bars in Figs. 2a–c).

The RMSEs of the six S2S models for the predicted weekly SAT anomaly against the observations over each of the three domains are shown in Figs. 2d–f. The RMSEs for all six S2S models are smaller for EISO-SJ-S summers than for EISO-SJ-W summers. Quantitatively, for a three-week lead prediction over the ETP, the RMSEs are 0.92 (ECMWF), 1.16 (CMA), 0.92 (Meteo-France), 1.03 (NCEP), 1.13 (ECCC), and 1.15 (ISAC-CNR) for EISO-SJ-S summers. In contrast, for EISO-SJ-W summers, the RMSEs are 0.96 (ECMWF), 1.18 (CMA), 1.03 (Meteo-France), 1.12 (NCEP), 1.14 (ECCC), and 1.16 (ISAC-CNR) (blue bars in Fig. 2d). Over the SWB, the increase in RMSEs from EISO-SJ-S summers to EISO-SJ-W summers is from 1.03 to 1.13 (ECMWF), 1.34 to 1.35 (CMA), 1.08 to 1.14 (Meteo-France), 1.13 to 1.27 (NCEP), 1.33 to 1.36 (ECCC), and 1.15 to 1.41 (ISAC-CNR) (blue bars in Fig. 2e). Over NC, the RMSEs are increased from 1.23 (ECMWF), 1.49 (CMA), 1.21 (Meteo-France), 1.30 (NCEP), 1.62 (ECCC), and 1.52 (ISAC-CNR) for EISO-SJ-S summers to 1.36 (ECMWF), 1.61 (CMA), 1.30 (Meteo-France), 1.42 (NCEP), 1.71 (ECCC), and 1.61 (ISAC-CNR) for EISO-SJ-W summers (green bars in Fig. 2f). Similarly, two-week lead predictions show similar contrasting features (yellow bars in Figs. 2d–f). The unified differences over the three regions for all six S2S models, based on both TCCs and

RMSEs, demonstrate that the deterministic prediction skills for the weekly SAT anomaly over EA are significantly better in summers with strong EISO-SJ intensity than in summers with weak EISO-SJ intensity.

4.2 Better subseasonal probabilistic prediction for EA SAT in summers with strong EISO-SJ intensity

The ROC curve is used to comprehensively evaluate model performance in simulating the probability of occurrence of above-normal SAT events. Here, an above-normal SAT event is defined as a weekly SAT warm anomaly of >1 °C (Wu et al. 2017). The ROC curves for the six S2S models for predicted above-normal SAT events over the ETP, SWB, and NC are shown in Fig. 3, respectively, in EISO-SJ-S and EISO-SJ-W summers. Obviously, the six S2S models have larger ROCAs for EISO-SJ-S summers than for EISO-SJ-W summers over each of the three regions. In terms of the three-week lead prediction over the ETP, the ROCAs are 0.62 (ECMWF), 0.57 (CMA), 0.65 (Meteo-France), 0.65 (NCEP), 0.61 (ECCC), and 0.61 (ISAC-CNR) for EISO-SJ-S summers, while 0.61 (ECMWF), 0.54 (CMA), 0.57 (Meteo-France), 0.60 (NCEP), 0.55 (ECCC), and 0.58 (ISAC-CNR) for EISO-SJ-W summers (green solid and dotted lines in Fig. 3a). Over the SWB, the ROCAs decrease from 0.64 (ECMWF), 0.57 (CMA), 0.59 (Meteo-France), 0.60 (NCEP), 0.66 (ECCC), and 0.56 (ISAC-CNR) for EISO-SJ-S summers to 0.52 (ECMWF), 0.52 (CMA), 0.52 (Meteo-France), 0.58 (NCEP), 0.45 (ECCC), and 0.55 (ISAC-CNR) for EISO-SJ-W summers (green solid and dotted lines in Fig. 3b). Over NC, the ROCAs decrease from 0.74 (ECMWF), 0.54 (CMA), 0.67 (Meteo-France), 0.65 (NCEP), 0.54 (ECCC), and 0.58 (ISAC-CNR) for EISO-SJ-S summers to 0.53 (ECMWF), 0.53 (CMA), 0.60 (Meteo-France), 0.55 (NCEP), 0.50 (ECCC), and 0.49 (ISAC-CNR) for EISO-SJ-W summers (green solid and dotted lines in Fig. 3c). The two-week lead ROCAs show similar differences between EISO-SJ-S and EISO-SJ-W summers (red solid and dotted lines in Fig. 3). We also performed similar analysis for below-normal and normal SAT events, and the results revealed similar differences (Fig. S4 in the supplementary materials). The results from the evaluation of probabilistic prediction also clearly exhibited that the prediction skills with two- and three-week lead times are evidently improved when EISO-SJ intensity is enhanced in summer.

4.3 Dependence of subseasonal prediction for EA SAT on the EISO-SJ is independent of ENSO/MJO/BSISO

Considering that subseasonal prediction for EA SAT is likely modulated by the mean state such as ENSO (Martin et al. 2019) and tropical intraseasonal oscillation such as the MJO (e.g., Liang and Lin 2017; Lin 2018) and BSISO (Wu et al. 2022), we reexamined the robustness of the above results by removing ENSO/MJO/BSISO-associated summers (Table S3 in the supplementary materials lists the new samples of each model after the elimination of ENSO/MJO/BSISO-associated summers). Excluding the impact from ENSO, MJO, and BSISO, the subseasonal prediction for SAT also exhibits better skill in EISO-SJ-S summers than in EISO-SJ-W summers (Figs. S5–6 in the supplementary materials). The results indicate that the strong dependence of subseasonal prediction for EA SAT on the EISO-SJ, identified as a new finding in this study, is independent of ENSO/MJO/BSISO.

Therefore, the high level of agreement among the six S2S models and three target regions, with respect to better prediction skill in summers with strong EISO-SJ intensity in comparison with that in summers with weak EISO-SJ intensity, strongly suggests that the amplified quasi-biweekly periodic signals along the SJ evidently increase the regional subseasonal predictability over EA.

5. Discussion

Previous studies reported that the EISO-SJ mainly features a zonal quasi-biweekly Rossby wave in boreal summer (Fujinami and Yasunari 2004; Yang et al. 2014, 2017). We therefore considered the empirical orthogonal function for the quasi-biweekly V200 over the SJ region in EISO-SJ-S and EISO-SJ-W summers, and regressed the corresponding quasi-biweekly V200 and 200 hPa wave activity flux on the first principal component, as shown in Figs. 4a and 4b, respectively. There are clear Rossby waves in both EISO-SJ-S and EISO-SJ-W summers along the SJ, but the stronger wave activity fluxes propagate eastward along the SJ toward EA, significantly enhancing the quasi-biweekly signals in that regions in EISO-SJ-S summers in comparison with those in EISO-SJ-W summers. Furthermore, the variances of quasi-biweekly SAT are larger over the ETP, SWB, and NC in EISO-SJ-S summers than in EISO-SJ-W summers (Fig. 4c). The results suggest that the quasi-biweekly Rossby wave and the associated energy dispersion along the SJ are enhanced (reduced) over EA in EISO-SJ-S (EISO-SJ-W) summers, causing stronger (weaker) quasi-biweekly periodic variations in the target regional SAT. This can explain why the two- and three-week lead predictions in the S2S hindcast are improved remarkably in EISO-SJ-S summers.

We also performed similar analysis for precipitation, but failed to find significant dependence on EISO-SJ (not shown). We investigated the reason why subseasonal prediction of EA precipitation might be insensitive to EISO-SJ intensity. Table S4 in the supplementary materials lists the fractional variances of quasi-biweekly and synoptic (i.e., below-8-day) components for SAT and precipitation over the ETP, SWB, and NC. Interestingly, for SAT, the fractional variance of the quasi-biweekly component is much larger than that of the synoptic component (e.g., the three region-averaged quasi-biweekly fractional variance is 39.1%, which is twice that of the synoptic component). For precipitation, however, the fractional variance of the quasi-biweekly component is smaller than that of the synoptic component (31.9% versus 39.2% on average). The above results indicate that the footprint of the atmospheric EISO-SJ on the subseasonal variation of precipitation is not as significant as that on the SAT over EA, which also suggests that subseasonal prediction for EA precipitation is more difficult than that for EA SAT.

6. Conclusions

Using hindcast data from six S2S models, this study found that the subseasonal prediction skill for EA SAT exhibits evident dependence on the intensity of intraseasonal variations along the SJ. In summers with strong EISO-SJ intensity, the two–three-week prediction skills for SAT over the ETP, SWB and NC are significantly better than those in summers with weak EISO-SJ intensity. Moreover, the strong dependence of subseasonal prediction for EA SAT on EISO-SJ intensity is proven independent of ENSO/MJO/BSISO. Further analysis indicated that the SJ-related quasi-biweekly Rossby wave and the associated energy dispersion are significantly strengthened downstream in strong EISO-SJ summers, resulting in stronger quasi-biweekly signals propagating toward EA. These enhanced periodic signals would cause more regular quasi-biweekly periodic variations in EA SAT, and increase regional subseasonal predictability. However, subseasonal prediction for EA precipitation is more difficult than that for EA SAT primarily because of the stronger internal synoptic variability. This study demonstrated that intraseasonal variations along the SJ provide a window of opportunity for subseasonal prediction of SAT over some regions of EA. Meanwhile, this study suggests that accurately capturing and predicting extratropical periodic atmospheric waves along the SJ in dynamic predictions will be of great importance for improving subseasonal prediction over EA.

Acknowledgments

JY and TZ were supported by funds from the National Natural Science Foundation of China (Grant No. 42022034) and the Key Collaborative Research Program of Alliance of International Science Organizations (Grant No. ANSO-CR-2020-01). The authors are grateful for the high-performance computing support from the Center for Geodata and Analysis, Faculty of Geographical Science, Beijing Normal University.

Data Availability Statement

The ERA-Interim reanalysis data can be freely accessed via http://apps.ecmwf.int/datasets/data/interim-full-daily/levtype=sfc/. The S2S hindcast data are available from https://apps.ecmwf.int/datasets/data/s2s/levtype=sfc/type=cf/. And the SAT and precipitation data recorded at 2479 observing stations are from http://data.cma.cn/en/?r=site/index (only available by the registered members), and are also obtained from the backup address (IP: 172.16.212.233:~/mnt/2479_station).

References

Black, J., Johnson, N. C., Baxter, S., Feldstein, S. B., Harnos, D. S., and L'Heureux, M. L. (2017). The Predictors and Forecast Skill of Northern Hemisphere Teleconnection Patterns for Lead Times of 3-4 Weeks. *Monthly Weather Review, 145*(7), 2855-2877. https://doi.org/10.1175/MWR-D-16-0394.1

Chan, J. C. L., Wi, W. X., and Xu, J. J. (2002). Mechanisms responsible for the maintenance of the 1998 South China Sea Summer Monsoon. *Journal of the Meteorological Society of Japan, 80*(5), 1103-1113. https://doi.org/10.2151/jmsj.80.1103

Dai, G. K., Mu, M., Li, C. X., Han, Z., and Wang, L. (2021). Evaluation of the Forecast Performance for Extreme Cold Events in East Asia With Subseasonal-to-Seasonal Data Sets From ECMWF. *Journal of Geophysical Research: Atmospheres, 126*(1). https://doi.org/10.1029/2020JD033860

Dee, D. P., et al. (2011). The ERA-Interim reanalysis: configuration and performance of the data assimilation system. *Quarterly Journal of the Royal Meteorological Society, 137*(656), 553-597. https://doi.org/10.1002/qj.828

Fujinami, H., and Yasunari, T. (2004). Submonthly variability of convection and circulation over and around the Tibetan Plateau during the boreal summer. *Journal of the Meteorological Society of Japan*, *82*(6), 1545-1564. https://doi.org/10.2151/jmsj.82.1545

Gao, M. N., Yang, J., Wang, B., Zhou, S. Y., Gong, D. Y., and Kim, S. J. (2018). How are heat waves over Yangtze River valley associated with atmospheric quasi-biweekly oscillation? *Climate Dynamics, 51*(11-12), 4421-4437. https://doi.org/10.1007/s00382-017-3526-z

Harnos, K. J., L'Heureux, M., Ding, Q., and Zhang, Q. (2019). Skill of Seasonal Arctic Sea Ice Extent Predictions Using the North American Multimodel Ensemble. *Journal of Climate*, *32*(2), 623-638. https://doi.org/10.1175/JCLI-D-17-0766.1

Leung, Y. F. (2012). Recreation ecology research in East Asia's protected areas: Redefining impacts? *Journal for Nature Conservation, 20*(6), 349-356. https://doi.org/10.1016/j.jnc.2012.07.005

Li, J. Y., Li, F., and Wang, H. J. (2020). Subseasonal prediction of winter precipitation in southern China using the early November snowpack over the Urals. *Atmospheric and Oceanic Science Letters, 13*(6), 534-541. https://doi.org/10.1080/16742834.2020.1824547

Li, J. Y., Zhai, P. M., Mao, J. Y., Song, L. L., and Xiao, Q. Y. (2021). Synergistic Effect of the 25-60-day Tropical and Midlatitude Intraseasonal Oscillations on the Persistently Severe Yangtze Floods. *Geophysical Research Letters, 48*(20). https://doi.org/10.1029/2021GL095129

Liang, P., and Lin, H. (2018). Sub-seasonal prediction over East Asia during boreal summer using the ECCC monthly forecasting system. *Climate Dynamics, 50*(3-4), 1007-1022. https://doi.org/10.1007/s00382-017-3658-1

Lin, H. (2018). Predicting the Dominant Patterns of Subseasonal Variability of Wintertime Surface Air Temperature in Extratropical Northern Hemisphere. *Geophysical Research Letters, 45*(9), 4381-4389. https://doi.org/10.1029/2018GL077509

Martin, G. M., Chevuturi, A., Comer, R. E., Dunstone, N. J., Scaife, A. A., and Zhang, D. Q. (2019). Predictability of South China Sea Summer Monsoon Onset. *Advances in Atmospheric Sciences, 36*(3), 253-260. https://doi.org/10.1007/s00376-018-8100-z

Merryfield, W. J., et al. (2020). Current and Emerging Developments in Subseasonal to Decadal Prediction. *Bulletin of the American Meteorological Society, 101*(6), E869-E896. https://doi.org/10.1175/BAMS-D-19-0037.1

Moon, J. Y., Wang, B., and Ha, K. J. (2011). ENSO regulation of MJO teleconnection. *Climate Dynamics, 37*(5-6), 1133-1149. https://doi.org/10.1007/s00382-010-0902-3

National Academies of Sciences, Engineering and Medicine. (2016). *Next generation Earth system prediction: Strategies for subseasonal to seasonal forecasts*. National Academies Press. https://doi.org/10.17226/21873

Orsolini, Y. J., Senan, R., Balsamo, G., Doblas-Reyes, F. J., Vitart, F., Weisheimer, A., Carrasco, A., and Benestad, R. E. (2013). Impact of snow initialization on sub-seasonal forecasts. *Climate Dynamics, 41*(7-8), 1969-1982. https://doi.org/10.1007/s00382-013-1782-0

Osman, M., and Alvarez, M. S. (2018). Subseasonal prediction of the heat wave of December 2013 in Southern South America by the POAMA and BCC-CPS models. *Climate Dynamics, 50*(1-2), 67-81. https://doi.org/10.1007/s00382-017-3582-4

Qi, X., and Yang, J. (2019). Extended-range prediction of a heat wave event over the Yangtze River Valley: role of intraseasonal signals. *Atmospheric and Oceanic Science Letters, 12*(6), 451-457. https://doi.org/10.1080/16742834.2019.1669408

Qin, M. Y., Li, S. L., Xue, Y. F., and Han, Z. (2022). Intraseasonal variability modes of winter surface air temperature over central Asia and their modulation by Greenland Sea ice and central Pacific El Nino-Southern Oscillation. *International Journal of Climatology*. https://doi.org/10.1002/joc.7691

Robertson, A. W., Kumar, A., Peña, M., and Vitart, F. (2015). Improving and promoting subseasonal to seasonal prediction. *Bulletin of the American Meteorological Society, 96*(3), ES49-ES53. https://doi.org/10.1175/BAMS-D-14-00139.1

Takaya, K., and Nakamura, H. (2001). A formulation of a phase-independent wave-activity flux for stationary and migratory quasigeostrophic eddies on a zonally varying basic flow. *Journal of the Atmospheric Sciences, 58*(6), 608-627. https://doi.org/10.1175/1520-0469(2001)058<0608:AFOAPI>2.0.CO;2

Teng, H. Y., and Wang, B. (2003). Interannual variations of the boreal summer intraseasonal oscillation in the Asian-Pacific region. *Journal of Climate, 16*(22), 3572-3584. https://doi.org/10.1175/1520-

0442(2003)016<3572:IVOTBS>2.0.CO;2

Vimont, D. J., Battisti, D. S., and Hirst, A. C. (2001). Footprinting: A seasonal connection between the tropics and mid-latitudes. *Geophysical Research Letters, 28*(20), 3923-3926. https://doi.org/10.1029/2001GL013435

Vitart, F., et al. (2017). The subseasonal to seasonal (S2S) prediction project database. *Bulletin of the American Meteorological Society, 98*(1), 163-173. https://doi.org/10.1175/BAMS-D-16-0017.1

Watanabe, T., and Yamazaki, K. (2012). Influence of the Anticyclonic Anomaly in the Subtropical Jet over the Western Tibetan Plateau on the Intraseasonal Variability of the Summer Asian Monsoon in Early Summer. *Journal of Climate*, *25*(4), 1291-1303. https://doi.org/10.1175/JCLI-D-11-00036.1

Watanabe, T., and Yamazaki, K. (2014). The upper-level circulation anomaly over Central Asia and its relationship to the Asian monsoon and mid-latitude wave train in early summer. *Climate Dynamics, 42*(9-10), 2477-2489. https://doi.org/10.1007/s00382-013-1888-4

Wu, J., Ren, H., Zhang, S., Liu, Y., and Liu, X. (2017). Evaluation and Predictability Analysis of Seasonal Prediction by BCC Second-Generation Climate System Model. *Chinese Journal of Atmospheric Sciences*, *41*(6), 1300-1315.

Wu, J. T., Li, J., Zhu, Z. W., and Hsu, P. C. (2022). Factors determining the subseasonal prediction skill of summer extreme rainfall over southern China. *Climate Dynamics*. https://doi.org/10.1007/s00382-022-06326-w

Xie, J. H., Yu, J. H., Chen, H. S., and Hsu, P. C. (2020). Sources of Subseasonal Prediction Skill for Heatwaves over the Yangtze River Basin Revealed from Three S2S Models. *Advances in Atmospheric Sciences*, *37*(12), 1435-1450. https://doi.org/10.1007/s00376-020-0144-1

Xue, Y. K., et al. (2021). Impact of Initialized Land Surface Temperature and Snowpack on Subseasonal to Seasonal Prediction Project, Phase I (LS4P-I): organization and experimental design. *Geoscientific Model Development, 14*(7), 4465-4494. https://doi.org/10.5194/gmd-14-4465-2021

Yan, Y. H., Liu, B. Q., and Zhu, C. W. (2021). Subseasonal Predictability of South China Sea Summer Monsoon Onset With the ECMWF S2S Forecasting System. *Geophysical Research Letters, 48*(24). https://doi.org/10.1029/2021GL095943

Yan, Y. H., Liu, B. Q., Zhu, C. W., Lu, R. Y., Jiang, N., and Ma, S. M. (2022). Subseasonal forecast barrier of the North Atlantic oscillation in S2S models during the extreme mei-yu rainfall event in 2020. *Climate Dynamics, 58*(11-12), 2913-2925. https://doi.org/10.1007/s00382-021-06076-1

Yang, J., Bao, Q., Wang, B., Gong, D. Y., He, H. Z., and Gao, M. N. (2014). Distinct quasi-biweekly features of the subtropical East Asian monsoon during early and late summers. *Climate Dynamics, 42*(5-6), 1469-1486. https://doi.org/10.1007/s00382-013-1728-6

Yang, J., Bao, Q., Wang, B., He, H. Z., Gao, M. N., and Gong, D. Y. (2017). Characterizing two types of transient intraseasonal oscillations in the Eastern Tibetan Plateau summer rainfall. *Climate Dynamics, 48*(5-6), 1749-1768. https://doi.org/10.1007/s00382-016-3170-z

Yang, L., and Zhang, Q. (2007). Anomalous Perturbation Kinetic Energy of Rossby Wave along East Asian Westerly Jet and Its Association with Summer Rainfall in China. *Chinese Journal of Atmospheric Sciences*, *31*(4), 586-595.

Zeng, D. W., and Yuan, X. (2018). Multiscale Land-Atmosphere Coupling and Its Application in Assessing Subseasonal Forecasts over East Asia. *Journal of Hydrometeorology*, *19*(5), 745-760. https://doi.org/10.1175/JHM-D-17-0215.1

Zhang, T. T., Huang, B. H., Yang, S., and Kinter, J. L. (2018). Predictable Patterns of the Atmospheric Low-Level Circulation over the Indo-Pacific Region in Project Minerva: Seasonal Dependence and Intraensemble Variability. *Journal of Climate, 31*(20), 8351-8379. https://doi.org/10.1175/JCLI-D-17-0577.1

Zhong, S. S., Wang, H., Chen, B., and Chen, H. (2022). Modulation of the Atmospheric Heat Source Over the Tibetan Plateau on the Intra-seasonal Oscillation of Summer Precipitation in the Yangtze-Huaihe River Basin. *Atmosphere-Ocean*, *60*(5), 600-612. https://doi.org/10.1080/07055900.2022.2077170

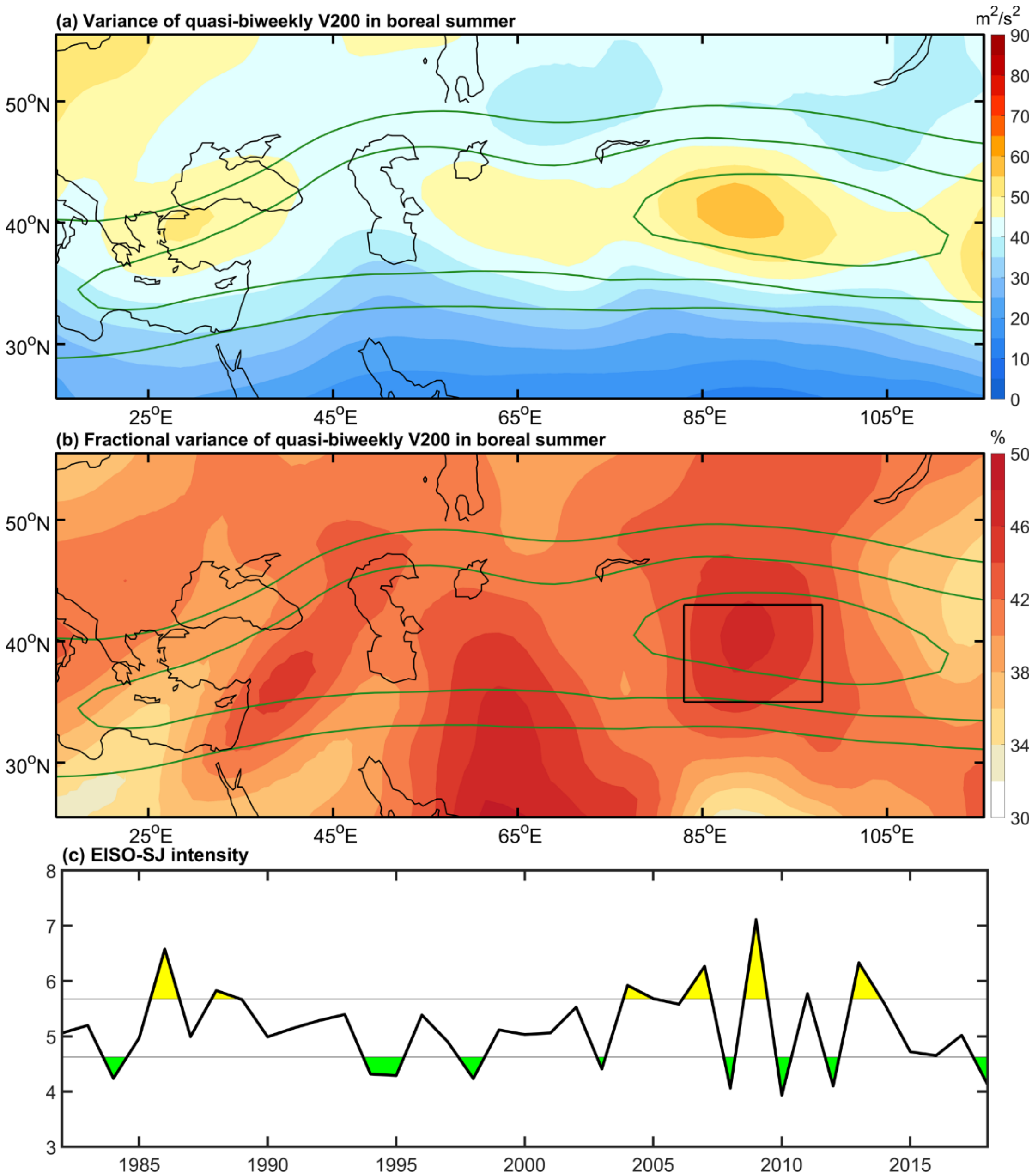

FIG. 1. (a) Variance (shading; unit: $m^2\ s^{-2}$) and **(b)** fractional variance (shading; unit: %) of quasi-biweekly V200 against total V200 variance in boreal summer. Green lines are the summer–mean U200 contour of 18, 23 and 28 m s^{-1}, which broadly denote the SJ's location. **(c)** Time series (unit: m s^{-1}) of domain-averaged quasi-biweekly V200 intensity over the SJ core region. Values greater (less) than 0.7 times the standard deviation are shaded yellow (green).

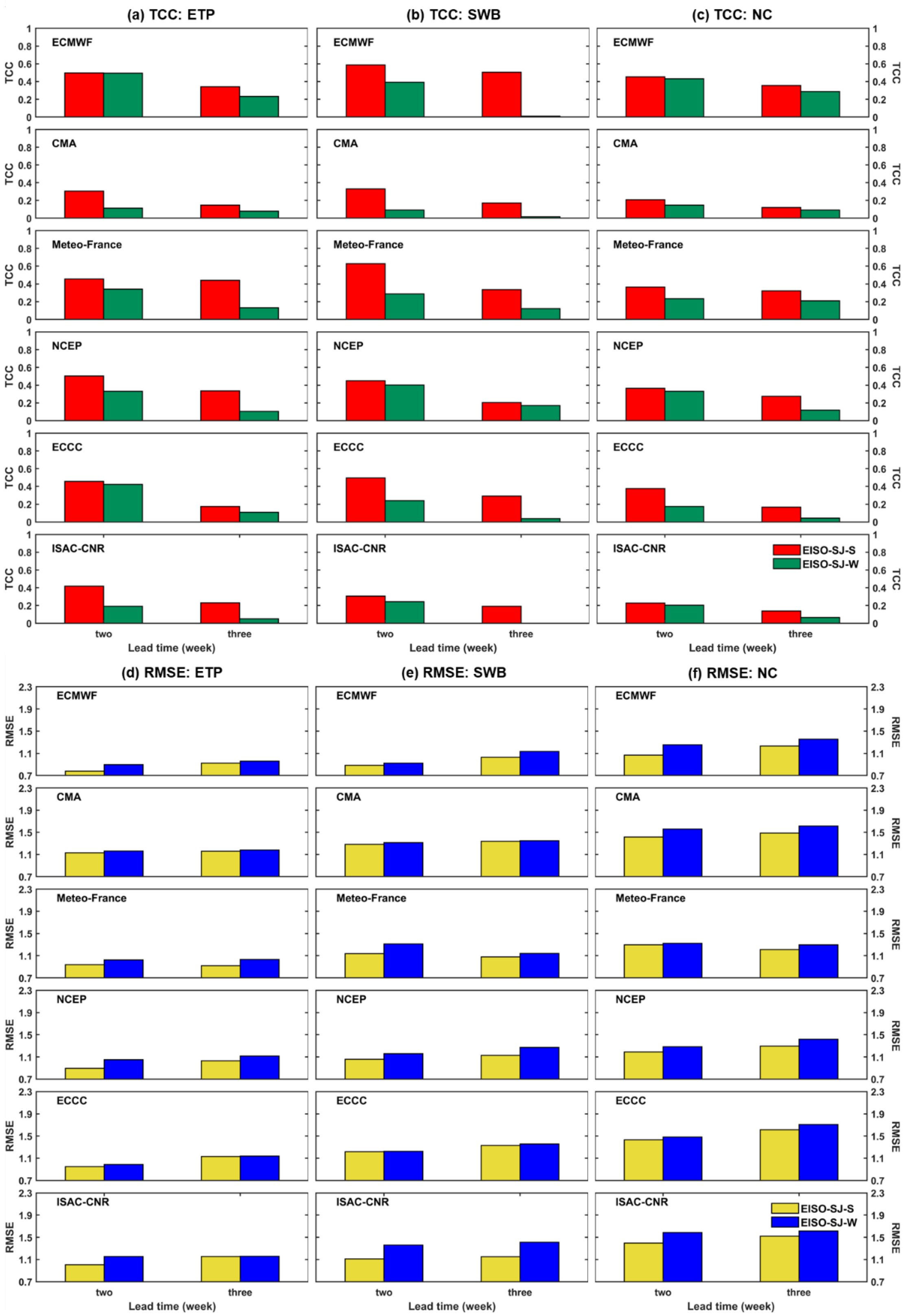

FIG. 2. Temporal correlation coefficient (TCC) between the observed weekly SAT anomaly and the predicted ensemble-mean weekly SAT anomaly over the **(a)** ETP, **(b)** SWB, and **(c)** NC with two- and three-week lead times. **(d–f)** As in **(a–c)**, but for Root Mean Square Error (RMSE).

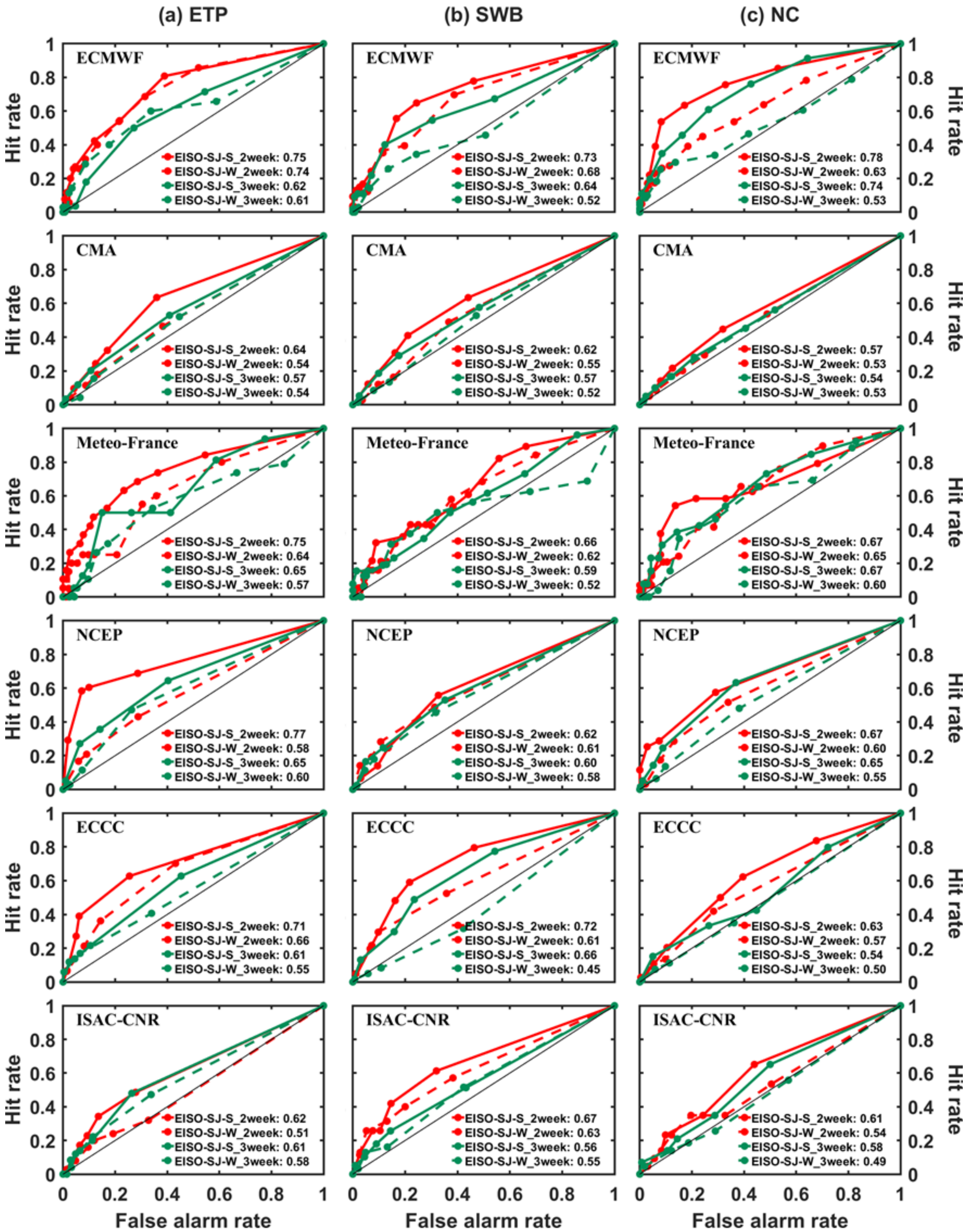

FIG. 3. Relative operating characteristics (ROC) curve for predicting above-normal SAT events over the **(a)** ETP, **(b)** SWB, and **(c)** NC from the six S2S models with two- and three-week lead times.

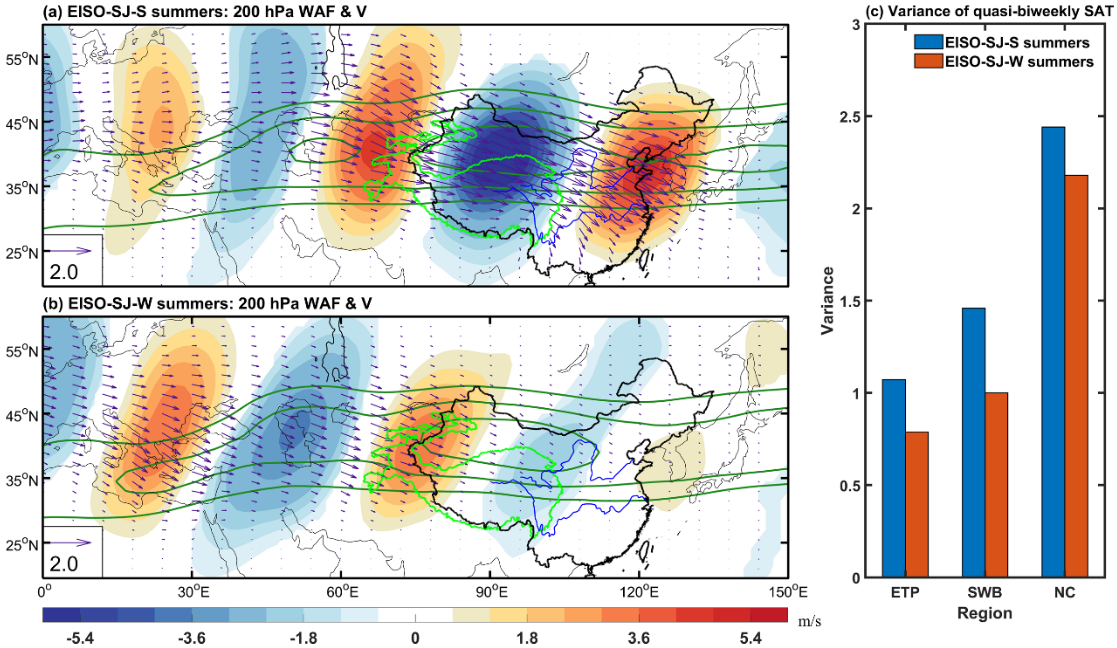

FIG. 4. Regression maps of boreal summer quasi-biweekly V200 (shading; unit: m s^{-1}) and 200 hPa wave activity flux (WAF; vectors; unit: m^2 s^{-2}) on the first principal component in **(a)** EISO-SJ-S and **(b)** EISO-SJ-W summers. Only values passing the 95% confidence level are plotted. **(c)** Variance of quasi-biweekly SAT over the ETP, SWB, and NC in EISO-SJ-S (blue bars; unit: °C^2) and EISO-SJ-W summers (orange bars; unit: °C^2).

Geophysical Research Letters

Supporting Information for【Extratropical intraseasonal signals along the subtropical westerly jet as a window of opportunity for subseasonal prediction over East Asia in boreal summer】

Tao Zhu[1,2]   Jing Yang[1,2]

[1] Key Laboratory of Environmental Change and Natural Disaster, Beijing Normal University, Beijing 100875, China

[2] Faculty of Geographical Science, Beijing Normal University, Beijing 100875, China

Submitted to GRL

Nov. 2022

**Corresponding author address: Jing Yang, Key Laboratory of Environmental Change and Natural Disaster, Faculty of Geographical Science, Beijing Normal University, 19#Xinjiekouwai Street, Haidian District, Beijing 100875, China. E-mail: yangjing@bnu.edu.cn*

1. Four Tables, six Figures, and two equations

Table S1. Description of the S2S models.

	Time range	Resolution	Re-forecast	Rfc length	Rfc frequency	Rfc size
CMA	Days 0–60	~1° × 1°, L40	Fixed	1994–2014	Daily	4
ECCC	Days 0–32	0.45° × 0.45°, L40	On the fly	1995–2014	Weekly	4
ECMWF	Days 0–46	T639/319 L91	On the fly	1996–2015	2/week	11
ISAC-CNR	Days 0–31	0.8° × 0.56°, L54	Fixed	1981–2010	Every 5 days	5
Meteo-France	Day 0–60	~0.5° × 0.8°, L85	On the fly	1993–2014	4/month	15
NCEP	Days 0–44	~1° × 1°, L64	Fixed	1999–2010	Daily	4

Table S2. ROC contingency table for defining event probabilistic prediction parameters.

Bin number	Prediction probabilities	Observed occurrences	Observed non-occurrences
1	$0–P_2$ (%)	O_1	NO_1
2	$P_2–P_3$ (%)	O_2	NO_2
3	$P_3–P_4$ (%)	O_3	NO_3
……	……	……	……
n	$P_n–P_{n+1}$ (%)	O_n	NO_n
……	……	……	……
N	$P_N–100$ (%)	O_N	NO_N

In ROC contingency table, *n* is the number of the n^{th} probability interval or bin *n*. *n* goes from *1* to *N*. *Pn* is the lower probability limit for bin *n*; P_{n+1} is upper probability limit for bin *n*; *N* is the number of probability intervals or bins. The prediction probabilities are the member sizes in each model that predict the event occurrence in this study.

$$O_n = \sum w_i(O)_i;\ NO_n = \sum w_i(NO)_i$$

where O_n/NO_n is the observed occurred/non-occurred frequency in n^{th} probability interval, i is the samples, and w_i is $\cos\theta_i$, representing the weight coefficient of the i^{th}, in which θ_i is the latitude of i^{th}. O_i is 1 when an event corresponding to a prediction in n^{th} probability interval, is observed as an occurrence, otherwise O_i is 0. NO_i is 1 when an event corresponding to a predicion in n^{th} probability interval, is not observed, otherwise NO_i is 0.

The curve formed by the hit rate (HR) and false alarm rate (FAR) is the ROC curve, in which the HR and FAR are calculated as

$$HR_n = \sum_{i=n}^{N} O_i / \sum_{i=1}^{N} O_i;\ FAR_n = \sum_{i=n}^{N} NO_i / \sum_{i=1}^{N} NO_i$$

Table S3. Sample sizes in EISO-SJ-S and EISO-SJ-W summers before and after removing the ENSO/MJO/BSISO-associated summers.

Name	EISO-SJ-S	EISO-SJ-W	Sample numbers for EISO-SJ-S and EISO-SJ-W	EISO-SJ-S⁻	EISO-SJ-W⁻	Sample numbers for EISO-SJ-S⁻ and EISO-SJ-W⁻
ERA-Interim	1986, 1988, 2004, 2005, 2007, 2009, 2011, 2013	1984, 1994, 1995, 1998, 2003, 2008, 2010, 2012, 2018	\	2005, 2009, 2013	1984, 1994, 1998, 2003, 2012, 2018	\
CMA	2004, 2005, 2007, 2009, 2011, 2013	1994, 1995, 1998, 2008, 2010, 2012	738 (6 year × 123 times year^{-1})	2005, 2009, 2013	1994, 1998, 2012	369 (3 year × 123 times year^{-1})
ECCC	2004, 2005, 2007, 2009, 2011, 2013	1995, 1998, 2003, 2008, 2010, 2012	102 (6 year × 17 times year^{-1})	2005, 2009, 2013	1998, 2003, 2012	51 (3 year × 17 times year^{-1})
ECMWF	2004, 2007, 2009, 2011, 2013	1998, 2003, 2008, 2010, 2012	175 (5 year × 35 times year^{-1})	2005, 2009, 2013	1998, 2003, 2012	105 (3 year × 35 times year^{-1})
ISAC-CNR	1986, 1988, 2004, 2005, 2007, 2009	1984, 1994, 1995, 1998, 2008, 2010	150 (6 year × 25 times year^{-1})	2005, 2009	1984, 1998	50 (2 year × 25 times year^{-1})
Meteo-France	2004, 2005, 2007, 2009, 2011, 2013	1994, 1995, 1998, 2008, 2010, 2012	96 (6 year × 16 times year^{-1})	2005, 2009, 2013	1994, 1998, 2012	48 (3 year × 16 times year^{-1})
NCEP	2004, 2007, 2009	2003, 2008, 2010	369 (3 year × 123 times year^{-1})	2009	2003	123 (1 year × 123 times year^{-1})

*EISO-SJ-S⁻ and EISO-SJ-W⁻ are the strong and weak EISO-SJ intensity summers, respectively, without the ENSO/MJO/BSISO-associated summers. ENSO-related summers are defined as the absolute values of the boreal summer averaged Oceanic Niño Index (ONI) index are larger than 0.5, MJO-related summers are that the absolute values of the normalized boreal summer averaged MJO amplitude, calculated by $\sqrt{RMM1^2 + RMM2^2}$, are large than 1, and BSISO-related summers are that the absolute value of the normalized boreal summer averaged BSISO amplitude (i.e., BSISO1 index), is large than 1. ONI index is obtained via https://origin.cpc.ncep.noaa.gov/products/analysis_monitoring/ensostuff/ONI_v5.php, RMM1 and RMM2 are via http://www.bom.gov.au/climate/mjo/, and BSISO1 index is via https://apcc21.org/ser/meth.do?lang=en.

Table S4. The fractional variance of quasi-biweekly and synoptic SAT and precipitation over the ETP, SWB and NC.

	SAT		**Precipitation**	
	quasi-biweekly	synoptic	quasi-biweekly	synoptic
ETP	36.0%	13.0%	35.2%	33.3%
SWB	45.3%	19.9%	33.3%	41.1%
NC	36.1%	23.2%	27.2%	43.1%

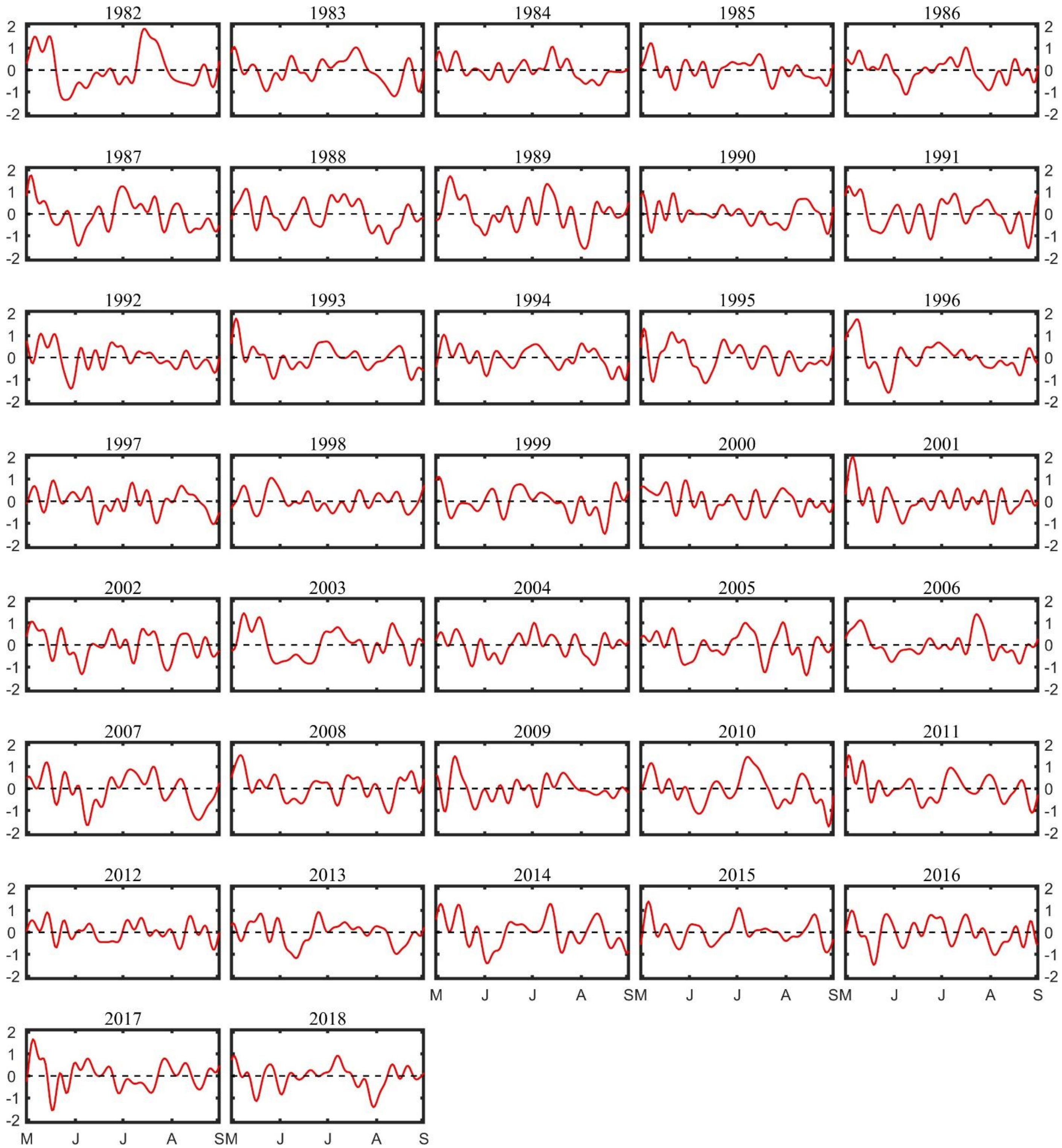

FIG. S1. Time series of the intraseasonal SJ index during each boreal summer (MJJA) of the 37 years.

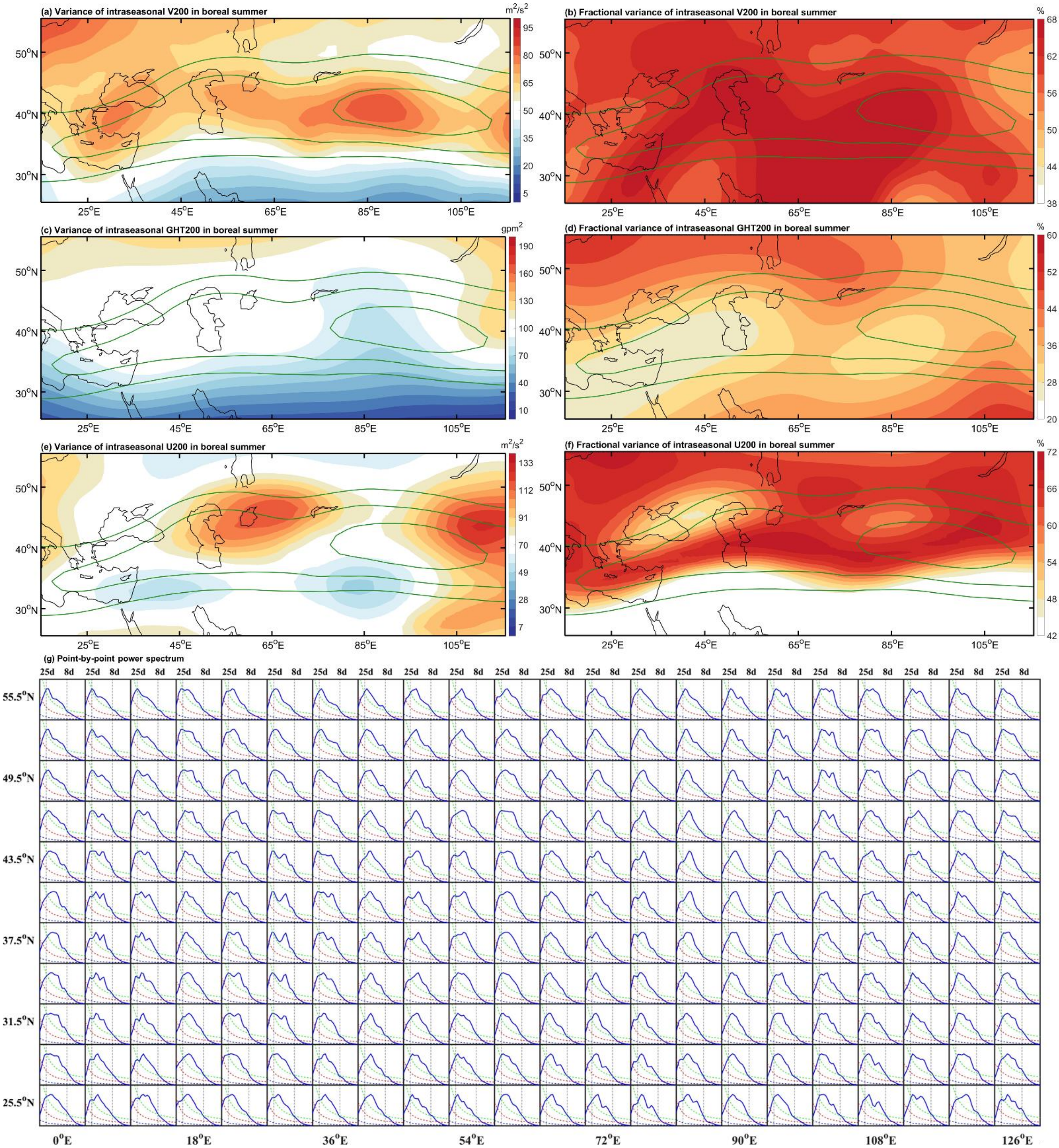

FIG. S2. (a) Variance (shading; unit: $m^2 s^{-2}$) and **(b)** fractional variance (shading; unit: %) of intraseasonal V200 against total V200 variance in boreal summer. Green lines are the summer–mean U200 contour of 18, 23 and 28 m s^{-1}, which broadly denote the SJ's location. **(c, d)**/**(e, f)** As in **(a, b),** but for GHT200/U200. **(g)** The point-by-point power spectrum of intraseasonal V200 over the SJ region. The red dashed line denotes the Markov red noise spectrum, and the blue/green dashed line represents the a priori/a posteriori 99% confidence. The grid point is chosen at intervals of 4.5 degrees of longitude and 3 degrees of latitude.

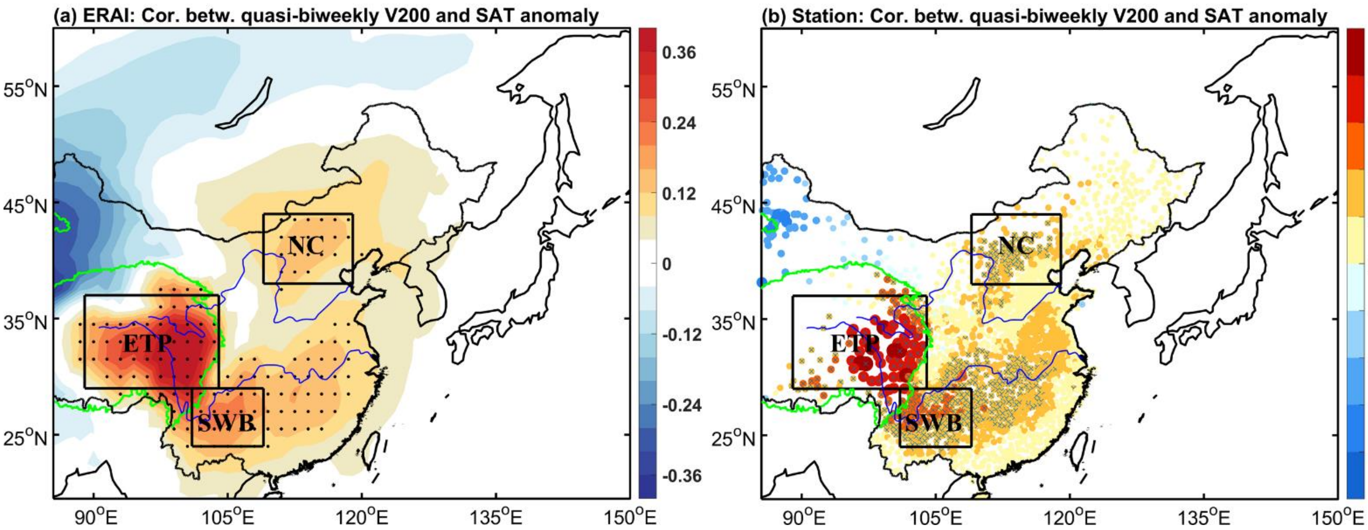

FIG. S3. Correlation coefficients (shading) between the quasi-biweekly V200 and anomalous SAT obtained from the **(a)** ERA Interim (ERAI) and **(b)** 2479-gauge stations. Black dots in **(a)** and blue "x" in **(b)** show the results above the 90% confidence level.

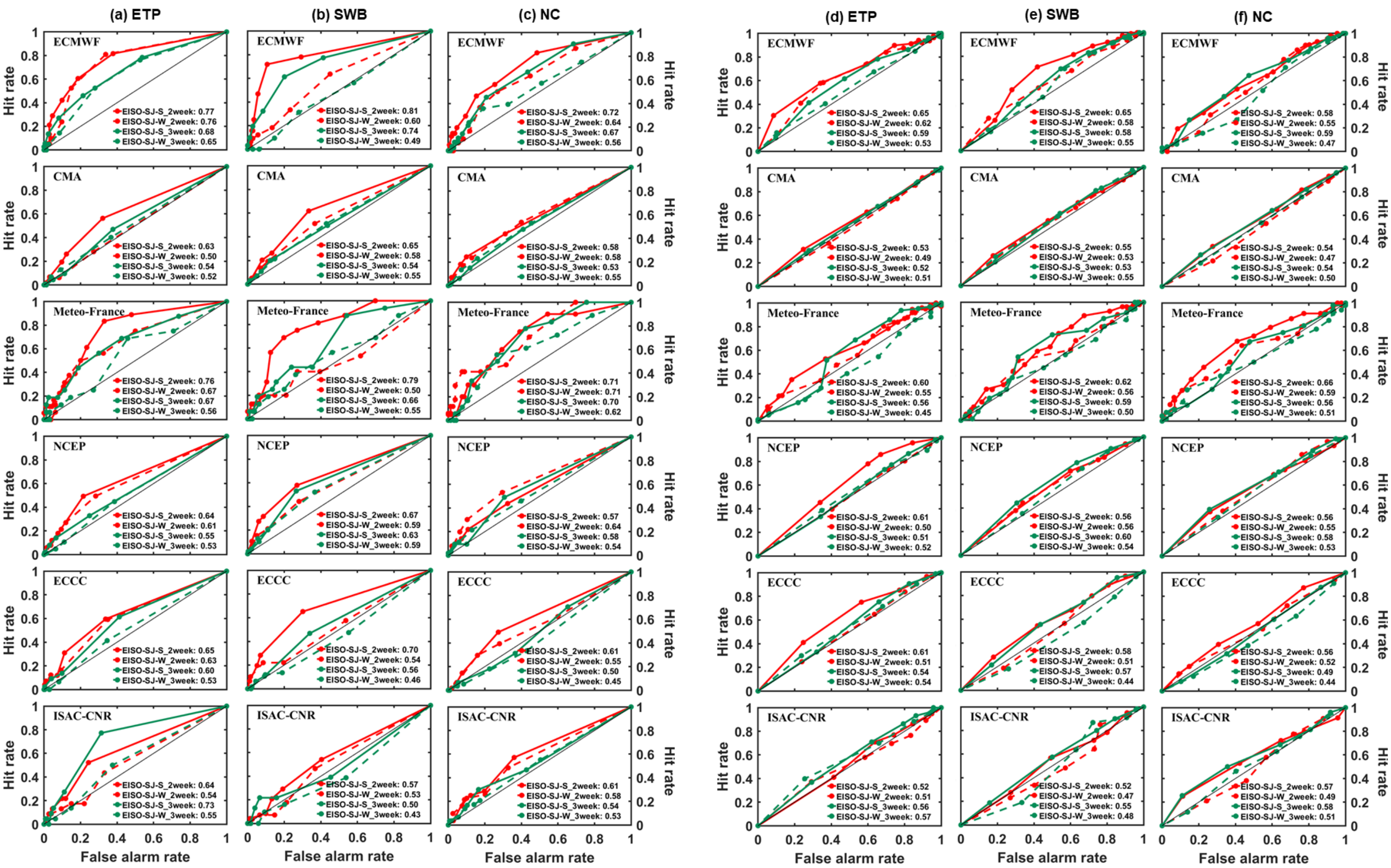

FIG. S4. Relative operating characteristics (ROC) curve for predicting below-normal SAT events over the **(a)** ETP, **(b)** SWB and **(c)** NC from S2S models with two- and three-week lead times. **(d–f)** As in **(a–c)**, but for normal SAT events. Here the below-normal SAT events are defined as the weekly SAT anomaly of <–1 °C, and the normal SAT event is the weekly SAT anomaly between –1 °C and 1 °C.

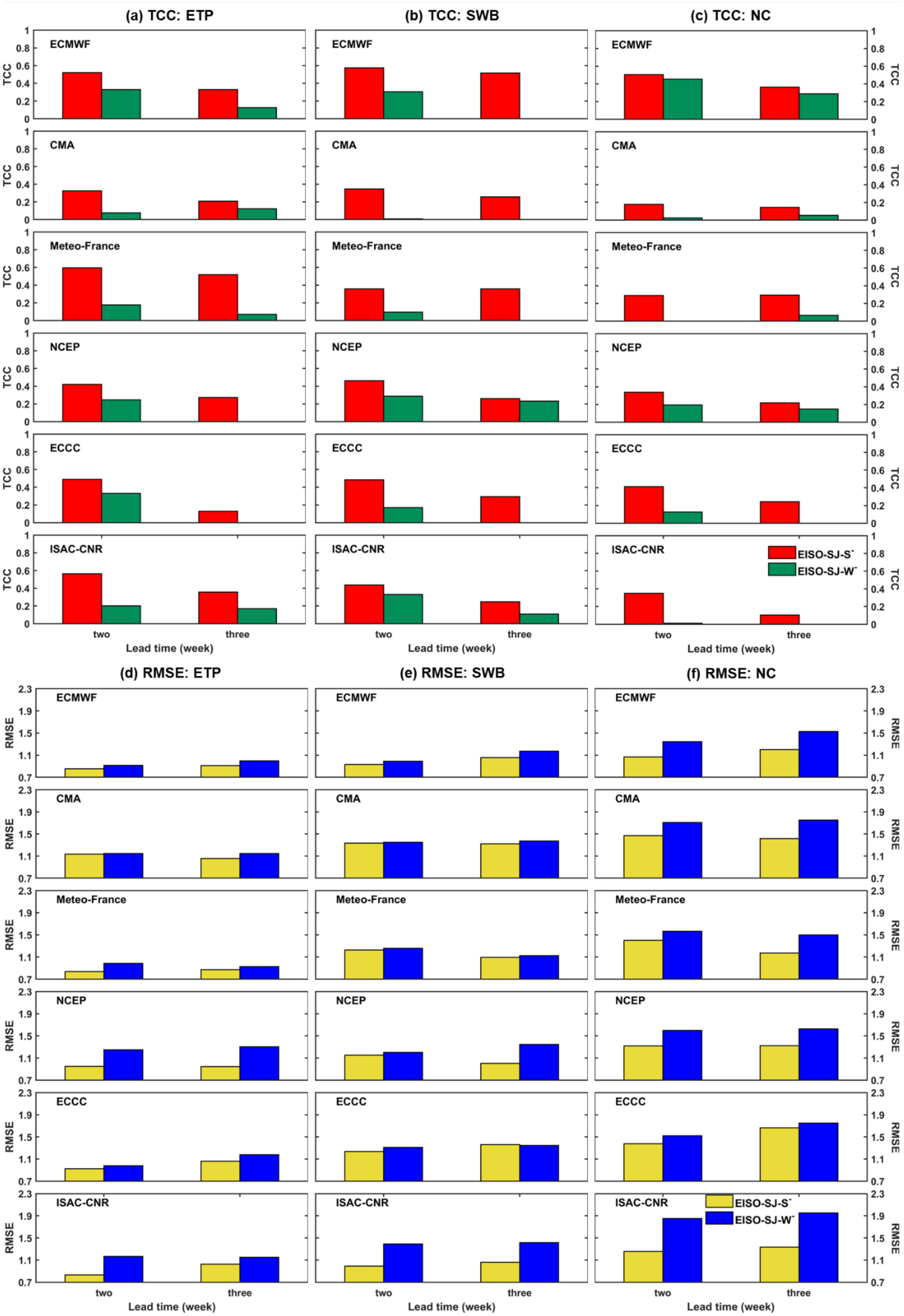

FIG. S5. Temporal correlation coefficient (TCC) between the observed weekly SAT anomaly and predicted ensemble-mean weekly SAT anomaly over the **(a)** ETP, **(b)** SWB and **(c)** NC with two- and three-week lead times. EISO-SJ-S^{-} and EISO-SJ-W^{-} samples are the prediction results in strong and weak EISO-SJ intensity summers, respectively, without the ENSO/MJO/BSISO-associated summers. **(d–f)** As in **(a–c)**, but for Root Mean Square Error (RMSE).

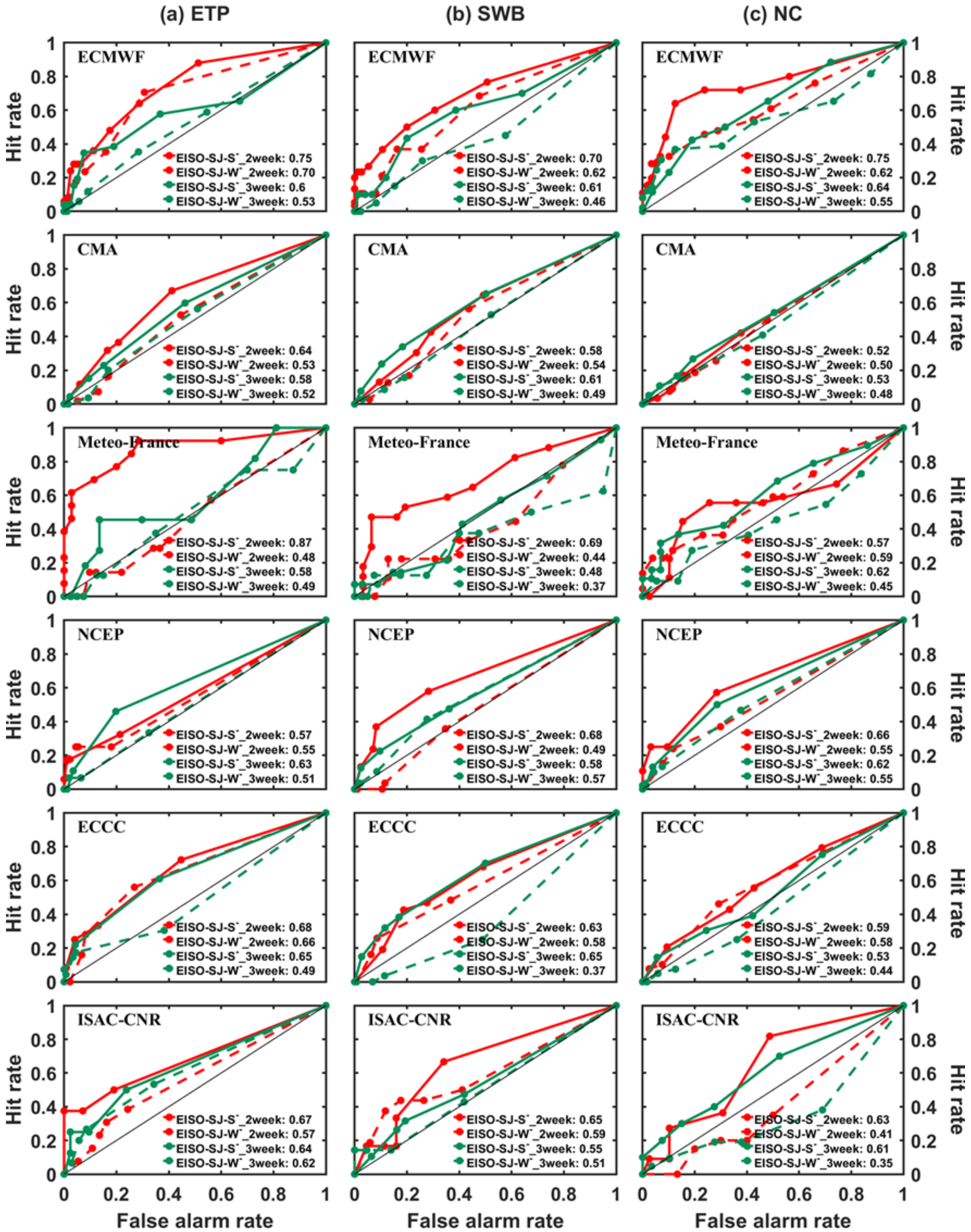

FIG. S6. ROC curve for predicting above-normal SAT events over the **(a)** ETP, **(b)** SWB and **(c)** NC from S2S models with two- and three-week lead times. EISO-SJ-S⁻ and EISO-SJ-W⁻ samples are the prediction results in strong and weak EISO-SJ intensity summers, respectively, without the ENSO/MJO/BSISO-associated summers.

$$TCC = \frac{\sum_{i=1}^{N}(x_i \times f_i)}{\sqrt{\sum_{i=1}^{N} x_i^2}\sqrt{\sum_{i=1}^{N} f_i^2}} \tag{S1}$$

$$\mathrm{RMSE} = \sqrt{\frac{1}{N}\sum_{i=1}^{N}(x_i - f_i)^2} \tag{S2}$$

where N, x_i and f_i are the sample numbers, observed and predicted ensemble-mean weekly anomaly (SAT & precipitation), respectively.